Free streamline detachment with surface tension: a conformal mapping-based numerical solution

Yuriy Semenov[1†], Baoyu Ni[1*†], M.G. Blyth[2†]

[1]College of Shipbuilding Engineering, Harbin Engineering University, Street, Harbin, 150001, State, China.
[2]School of Mathematics, University of East Anglia, Street, Norwich, NR4 7TJ, State, UK.

*Corresponding author(s). E-mail(s): nibaoyu@hrbeu.edu.cn;
Contributing authors: yuriy.a.semenov@gmail.com; M.Blyth@uea.ac.uk;
†The authors contributed equally to this work.

Abstract

The problem of the detachment of a free-streamline from a smoothly shaped body is considered taking into account the effect of surface tension. The fluid is assumed to be inviscid and incompressible, and the flow is assumed to be irrotational and stationary in the body-fixed frame but corresponds to a progressive capillary waves in the freestream frame. We employ the Brillouin-Villat criterion to determine the position of the free-streamline detachment. Using the integral hodograph method, we derive expressions for the complex velocity and the derivative of the complex potential, both defined in an auxiliary parameter plane. A system of singular integral equations, formulated in terms of the velocity magnitude along the free surface and the slope of the body, is derived by applying the dynamic and kinematic boundary conditions. The numerical method is highly efficient, as it only requires the evaluation of these two nonsingular functions. Numerical results demonstrate the effect of surface tension on the free-streamline detachment, the drag force and the free surface shape for a wide range of Weber numbers. It is shown that the surface tension generates capillary waves due to the distortion of the magnitude of the inflow velocity at the detachment point.

Keywords: Brillouin-Villat criterion for free-streamline detachment, Capillary water waves, Conformal mapping, Fully nonlinear computations

1 Introduction

Flows involving free-streamline detachment are encountered in high-speed fluid-structure interactions such as impact, cavity, and gliding flows, where inertial effects dominate over viscous or wettability forces. At sufficiently high Reynolds numbers, flow separation from a solid body can be modeled by inviscid theory with surface tension. Experiments by Duez et al. [15] showed that above a critical impact velocity, wettability and viscosity play a negligible role in the detachment process, emphasizing the importance of inertia and surface tension in such flows.

Classical studies of free-surface flows with capillarity can be traced back to Rayleigh and Kelvin (see Lamb [25], p. 455), and Joukovskii [21] (see Gurevich [19], p. 549), with applications ranging from water waves to bubble and cavity flows. Early work by Joukowskii incorporated surface tension into Bernoulli's equation, yielding fully nonlinear solutions for flows such as a bubble between parallel plates. Subsequent efforts extended the method to flows past cylindrical shells and bubbles by McLeod [28], and exact solutions were developed for capillary wave trains in irrotational flows of infinite depth by Crapper [7].

In recent decades significant progress has been made in understanding capillary-gravity waves [12, 13], though most of this work focused on traveling or standing waves rather than flow detachment phenomena. In contrast, the role of surface tension in the detachment mechanism remains less well understood. Classical potential theory predicts singular behavior at sharp edges, including infinite curvature and pressure. Even small amounts of surface tension lead to unbounded negative pressure at the trailing edge, seemingly precluding detachment. Dias and Kharif [14] provided a comprehensive review, emphasizing the bifurcation, stability, and evolution of capillary-gravity waves.

A number of analytical and numerical studies [1, 11, 18] have addressed surface tension corrections to classical Kirchhoff-type flows. Perturbation methods and matched asymptotic expansions have been used to regularize the edge singularity and describe the onset of capillary waves. Notably, Gurevich [18], Ackerberg [1], Zhitnikov [39] and others demonstrated the appearance of stationary capillary ripples near the detachment point.

For smoothly shaped bodies the mathematical solution can be constructed with the detachment point located anywhere along the body. To identify a solution that more accurately reflects real-world conditions, Brillouin [5] introduced criteria based on physical principles. The first Brillouin criterion states that, in the absence of surface tension, the pressure on the cavity boundary must be lower than or equal to the pressure on the body. The second Brillouin criterion asserts that the curvature of the free streamline must be finite to prevent it from penetrating the solid body. Villat [36] provided a rigorous mathematical formulation of this condition, demonstrating that when the curvature of the free surface at the detachment point is finite, it equals the curvature of the body at that point. For this reason the second Brillouin criterion is also referred to as the Brillouin-Villat criterion.

Since the second Brillouin criterion is inherently geometrical, it should remain valid in the presence of surface tension, a point that we shall exploit in the present work. While the Brillouin criteria are ad hoc and may be inaccurate when accounting

for viscosity, turbulence, or other fluid properties and flow conditions, they can serve as a useful first approximation for predicting the position of flow detachment caused by fluid inertia. Additionally, they provide valuable insights into the flow detachment mechanism in low-viscosity fluids, particularly when the effects of a boundary layer are considered ([38]).

Yoon and Semenov [37] derived a complex velocity potential for the cavity flow with surface tension by applying integral hodograph method (IHM). They reduced the problem to a system of singular integral equations and applied a method of successive approximations to solve it. However, in order to achieve convergence they introduced a restriction which requires monotonic behaviour of the unknown functions. This restriction was in line with the common theoretical point of view on detached flows with surface tension, but not justified mathematically and not confirmed by real observations. **here**

Numerical methods based on complex functions efficiently solve free-surface potential flow problems because these functions inherently satisfy the Laplace equation. The primary task involves identifying such a complex function that satisfies given boundary conditions. For simple geometries and straightforward boundary conditions, such as polygon-shaped bodies or uniform velocities at the free surface, complex function-based methods can provide fully analytical solutions. With advancements in computational resources, these methods have been further developed to effectively handle more complicated problems involving complex geometries and additional physical effects influencing boundary conditions, such as gravity, surface tension, and elastic boundaries, etc. Chalikov and Sheinin [6] developed a fully nonlinear complex function-based numerical model capable of directly simulating one-dimensional nonlinear gravity and gravity-capillary periodic waves. Clamond and Dutykh created a highly efficient and precise conformal mapping-based algorithm for modeling solitary waves [9, 16], subsequently expanding it to simulate Stokes waves at arbitrary water depths [10, 17]. Murashige and Choi [29] introduced the Unsteady Transformation Method to analyze transient parasitic capillary waves occurring at the front face of steep gravity waves. Akselsen [3] further advanced the conformal mapping approach, significantly improving computational efficiency and accuracy when simulating water wave interactions under complex and transient boundary conditions.

In this study, we revisit Kirchhoff flows with infinite cavities, focusing on the influence of surface tension on the detachment angle and free-surface shape. We use a body-fixed frame of reference which simplifies the analysis of a progressive capillary wave on the cavity surface to a steady flow. Building on the integral hodograph method [37], we apply a numerically efficient scheme based on the collocation method to solve the system of singular integral equations without any restriction on the unknown velocity magnitude along the free surface. We also develop a numerical model to resolve the singularity at the detachment point and provide an extensive convergence study.

The obtained results reveal qualitatively new effects of surface tension on the free-surface shape and more accurately predict the position of the free-streamline detachment. The remainder of the paper is organized as follows. Section 2 presents the mathematical formulation, nondimensionalization, and derivation of the integral

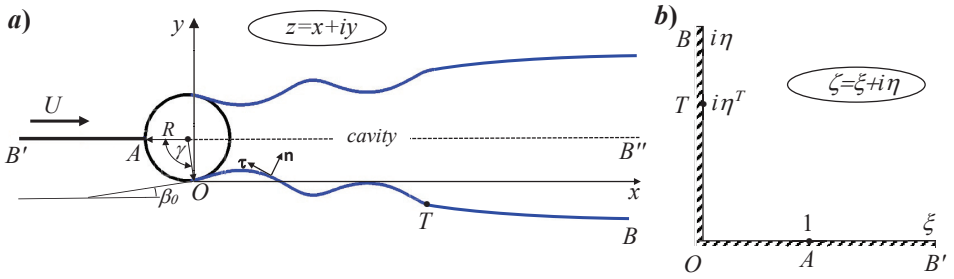


Fig. 1 (a) Sketch of the free-streamline flow past a cylinder, and (b) the parameter plane. Due to the flow symmetry about the $x-$axis, only the flow in the lower half-plane is considered.

equations. Section 3 describes the numerical solution strategy, including mesh refinement and convergence tests. In Section 4, we investigate the surface tension effects for various Weber numbers and geometries. Finally, conclusions are drawn in Section 5.

2 Formulation of the problem.

We study a two-dimensional irrotational free-streamline flow of an inviscid, incompressible fluid past either a circular cylinder or a flat plate with rounded edges. The case of the flow past a cylinder is sketched in figure 1a. Gravity is neglected, but surface tension is considered. The radius of the cylinder is denoted by R and we introduce a Cartesian coordinate system XY, with the origin at the detachment point O on the cylinder. The flow is symmetric with respect to the line $B'AB''$ as shown in figure 1a. The $X-$axis is aligned with the inflow velocity U, while the Y-axis points vertically upward. In this reference frame, there exists a steady motion of the liquid in which the free-surface contour remains fixed. In the alternative reference frame of the freestream, however, the free surface is carried along with the body, and its position depends on both spatial coordinates and time, thereby complicating the analysis.

Flow detachment occurs at point O on the cylinder, forming a free-streamline OTB, which extends to infinity. Surface tension may generate waves on the free surface, extending downstream to infinity. To satisfy the radiation condition, we apply the dynamic boundary condition on the segment OT of the free-streamline. On the remaining part of the streamline, TB, the velocity magnitude remains constant and equal to the inflow velocity U. The distance to point T can be as large as desired to eliminate its influence on the flow near the cylinder, but it must remain finite. This flow scheme, with an infinite detachment region, resembles the Kirchhoff flow for the case of a shaped body.

In the general case, the shape of the body is defined by the functions $X_b(S)$ and $Y_b(S)$, where S is the arc length coordinate ($S = 0$ at point O) , or by the slope of the cylinder, $\delta_b(S) = \arctan\left(dY_b/dX_b\right)$. The arc length coordinate S increases as we move, with the fluid on our left, from point B to point O along the free-streamline, and then from O to A along the cylinder, and from A to B' along the line of symmetry.

We introduce the complex velocity potential, $W(Z) = \Phi(X, Y) + i\Psi(X, Y)$, where $\Phi(X, Y)$ is the velocity potential and $\Psi(X, Y)$ is the streamfunction, and $Z = X + iY$.

The boundary-value problem for the velocity potential can be formulated as follows:

$$\nabla^2\Phi = 0, \quad \nabla^2\Psi = 0 \tag{1}$$

in the liquid domain;

$$\frac{\partial\Phi}{\partial Y} = \frac{\partial\Phi}{\partial X}\frac{dY_b}{dX_b}, \quad \Psi = 0 \tag{2}$$

on the body surface $(X_b(S), Y_b(S))$ and the streamline AB';

$$\frac{\rho V^2}{2} + p = \frac{\rho U^2}{2} + p_\infty, \quad \Psi = 0, \quad X_O < X(S) < X_T, \quad Y = Y(S), \tag{3}$$

which is the dynamic boundary condition on the part OT of the free-streamline, $Y = Y(S)$. Here $V = |\nabla\Phi|$ is the velocity magnitude, $p(X)$ is the hydrodynamic pressure on the liquid side of the free-streamline, and p_∞ is the pressure in the liquid at infinity; ρ is the density of the liquid;

$$p = p_\infty, \quad \Psi = 0, \quad X_T < X(S) < \infty, \quad Y = Y(S), \tag{4}$$

which is the dynamic boundary condition on the remaining part TB of the free-streamline; and the far-field condition

$$\nabla\Phi \to U, \quad |X^2 + Y^2| \to \infty. \tag{5}$$

To complete the formulation of the boundary-value problem (1)-(5), an equation for the hydrodynamic pressure at the free-streamline is needed. The surface tension affects the pressure jump across the free-streamline according to the Laplace-Young condition:

$$p - p_c = \tau K^*, \tag{6}$$

where p_c is the pressure inside the cavity, τ is the coefficient of surface tension and K^* is the curvature of the free-streamline. In Kirchhoff-type flows with an infinite cavity, the curvature of the free streamlines approaches zero at infinity; therefore, the pressure within the cavity is the same as the fluid pressure at infinity, $p_c = p_\infty$.

To prepare to solve the problem it is convenient to non-dimensionalize the variables. The velocity U and the half width of the body H are used as the reference velocity and length scales respectively. In the case of the circular cylinder, $H = R$, and $r = R/H = 1$. Specifically, we define $x = X/H$, $y = Y/H$, $s = S/H$, the body profile $x_b(s) = X_b(S)/H$ and $y_b(s) = Y_b(S)/H$, and the interface profile $x(s) = X(S)/H$ and $y(s) = Y(S)/H$. The non-dimensional curvature of the cylinder is given by $\kappa_b = d\delta_b/ds$, where $\delta_b(s) = \arctan(dy_b/dx_b)$.

The velocity potential Φ and the streamfunction Ψ are normalized to the product UH. The normalized variables are denoted as $\phi = \Phi/UH$ and $\psi = \Psi/UH$. With these normalizations, the value of the streamfunction on the free-streamline is $\psi = 0$.

By substituting (6) into the Bernoulli equation (3), the non-dimensional dynamic boundary condition takes the form

$$v = \frac{V}{U} = \sqrt{1 - \frac{2\kappa}{r\mathrm{We}}}, \tag{7}$$

where $v = V/U$ is the dimensionless velocity, $\kappa = K^*H$ is the dimensionless curvature of the free streamline, and We is the Weber number defined as follows:

$$\mathrm{We} = \frac{\rho U^2 H}{\tau}. \tag{8}$$

2.1 Complex Potential of the Free-Streamline Flow

Helmholtz [20] was the first to introduce a complex variable method for solving problems in fluid mechanics, while Kirchoff [23] proposed a conformal mapping technique for analyzing free streamline flow over a plate. This technique involves constructing conformal mappings using basic complex functions, making it somewhat heuristic for solving free surface and interface problems. Consequently, finding the complex potential function $w(z)$ can be a complicated task.

To develop a conformal mapping technique, Joukowskii [22] and Michell [26] introduced the concept of an auxiliary parameter plane, or ζ-plane, and sought two functions of the parameter variable ζ, one being the complex velocity dw/dz, and the other being the complex potential $w(\zeta)$, or its derivative, $dw/d\zeta$. Once these functions are identified, the velocity field can be determined as a function of the parameter variable ζ using the formula:

$$v_x - iv_y = \frac{dw}{dz}(\zeta) = ve^{i\chi}. \tag{9}$$

Here $\chi = -\beta$ is the argument of the complex conjugate velocity, and the β is the angle of the velocity with respect to the x-axis. The relationship between the parameter plane ζ and the physical plane z is established as the integral of the ratio between the derivative of the complex potential and the complex velocity, expressed as follows:

$$z(\zeta) = z_0 + \int_0^{\zeta} \frac{dz}{d\zeta'}\, d\zeta', \tag{10}$$

where z_0 in the physical plane corresponds to the point $\zeta = 0$ in the parameter plane. The function $z = z(\zeta)$ maps the parameter plane onto the physical plane and is referred to as the mapping function.

The Joukowski-Michell method is applicable for flows over polygon-shaped bodies with a constant velocity on the free surface. In this case, the range of variation of the functions

$$\omega = \ln\left(\frac{1}{v_0}\frac{dw}{dz}\right) = \ln\left(\frac{v}{v_0}\right) - i\beta, \tag{11}$$

and the complex potential $w(\zeta)$ are polygon-shaped regions; here, v_0 is the velocity magnitude at the point O. If the upper half-plane is chosen as the parameter region, then the functions $\omega(\zeta)$ and $w(\zeta)$ can be determined using the Schwarz-Christoffel integral, which conformally maps the upper half-plane onto the interior of the polygon in the ω- and w-planes, respectively.

Although the Joukowski-Michell method significantly extends the range of free-surface problems for which analytic solutions can be obtained, it still necessitates an explicit conformal mapping procedure. In some cases, evaluating the Schwarz-Christoffel integral can present difficulties.

The next significant advancement in the methodology for solving two-dimensional free-boundary problems was made by Chaplygin (see Chap. 1(5) in [19]). He developed a technique known as the method of special points, which enables the derivation of the desired complex function without relying on any explicit conformal mapping techniques. This method involves analyzing the behavior of the desired complex-variable function and identifying all its zeros and singularities within the flow domain, as well as in the region of the parameter variable ζ. Next, it is essential to extend the complex function across the entire ζ-plane and locate all its zeros and singularities using the Riemann-Schwarz symmetry principle ([27]). Once this is done, the desired complex function can be constructed from its zeros and poles using Liouville's theorem. Gurevich [19] noted the considerable flexibility in choosing the region of the parameter variable ζ. Typically, these regions can take the form of a half-plane, a quadrant, a circle, a semi-circle, a band, a half-strip, a rectangle, and so on. The only requirement is that these regions should be able to cover the entire complex plane through straightforward image transformations.

An additional complexity arises when the slope of the body varies along its contour or when the velocity magnitude on the free surface changes due to factors such as gravity, surface tension, etc. This leads to a mixed boundary value problem: on the solid part of the boundary the velocity direction is dictated by the slope of the body, while on the free surface the velocity magnitude can be determined using the Bernoulli equation. To ascertain the complex velocity function we require an integral formula that defines a complex function based on its boundary conditions.

Let us assume that the magnitude of the velocity, $v(\eta) = \left|\frac{dw}{dz}\right|$, is known as a function of the coordinate η along the imaginary axis in the ζ-plane, which corresponds to the free streamline OTB. Additionally, the argument of the complex velocity, $\chi(\xi) = \arg\left(\frac{dw}{dz}\right)$, is a known function of the coordinate ξ along the real axis in the ζ-plane. Using these definitions, we can formulate the following boundary-value problem for the complex velocity in the first quadrant:

$$\left|\frac{dw}{dz}\right|_{\zeta=i\eta} = v(\eta), \quad 0 < \eta < \infty, \quad \xi = 0. \tag{12}$$

$$\arg\left(\frac{dw}{dz}\right) = \chi(\xi), \quad 0 < \xi < \infty, \quad \eta = 0. \tag{13}$$

By employing Chaplygin's special point method ([19]), the following integral formula has been derived ([30]; [31]) for solving the mixed boundary value problem defined by

equations (12) and (13) in the first quadrant:

$$\frac{dw}{dz} = v_\infty \exp\left[-\frac{1}{\pi}\int_\infty^0 \frac{d\chi}{d\xi}\ln\left(\frac{\zeta+\xi}{\zeta-\xi}\right)d\xi - \frac{i}{\pi}\int_0^\infty \frac{d\ln v}{d\eta}\ln\left(\frac{\zeta-i\eta}{\zeta+i\eta}\right)d\eta + i\chi_\infty\right], \tag{14}$$

where $v_\infty = \lim_{\eta\to\infty} v(\eta)$ and $\chi_\infty = \lim_{\xi\to\infty}\chi(\xi)$ represent the velocity magnitude and direction at infinity (point BB'). It can be easily verified that, for $\zeta = \xi$, the argument of equation (14) corresponds to the function $\chi(\xi)$, and, for $\zeta = i\eta$, the magnitude of equation (14) corresponds to the function $v(\eta)$. This shows that the boundary conditions given by equations (12) and (13) are satisfied.

We chose the first quadrant as the region of the parameter variable $\zeta = \xi + i\eta$ as depicted in figure 1(b), which corresponds to the liquid domain in the physical plane $z = x + iy$ shown in figure 1(a). The interval $(0, 1)$ of the real axis corresponds to the cylinder surface OA, while the remainder of the real axis $(1, \infty)$ corresponds to segment AB' in the z-plane. The interval $(0, \infty)$ on the imaginary axis corresponds to the free streamline OTB. The conformal mapping theorem permits us to arbitrarily select the position of the images of three points: O ($\zeta = 0$), A ($\zeta = 1$), and BB' ($\zeta = \infty$), as shown in figure 1(b).

The functions $v(\eta)$ and

$$\chi(\xi) = \begin{cases} -\beta(\xi), & 0 \le \xi \le 1, \\ 0, & 1 \le \xi < \infty \end{cases} \tag{15}$$

are unknown *a priori*; these functions will be determined later using the dynamic and kinematic boundary conditions. Here $\beta(\xi)$ represents the velocity direction on the cylinder surface. At the point $\xi = 1$ there is a discontinuity in the function $\chi(\xi)$, given by $\Delta\chi_A = -\pi/2$, since $\lim_{\xi\to 1-0}\beta(\xi) = -\pi/2$. Since function $\beta(\xi)$ differs from the function $\delta_b(\xi)$ only by a constant π, we have $d\beta/d\xi = d\delta_b/d\xi$. Substituting (15) into (14), evaluating the integrals over the discontinuities in the function $\chi(\xi)$ and using the relation $d\beta/d\xi = d\delta_b/d\xi$, we derive the expression for the complex velocity as

$$\frac{dw}{dz} = v_0\sqrt{\frac{1-\zeta}{1+\zeta}}\exp\left[\frac{1}{\pi}\int_0^1 \frac{d\delta_b}{d\xi}\ln\left(\frac{\xi-\zeta}{\xi+\zeta}\right)d\xi - \frac{i}{\pi}\int_0^\infty \frac{d\ln v}{d\eta}\ln\left(\frac{i\eta-\zeta}{i\eta+\zeta}\right)d\eta - i\beta_0\right], \tag{16}$$

where β_0 is the velocity direction at the point of detachment O.

An explicit expression for the derivative of the complex potential can be derived using the conformal mapping method, as the region of the complex potential w is confined to the lower half-plane of the w-plane, i.e., $-\infty < \phi < \infty$, $-\infty < \psi \le 0$. The function $w = K\zeta^2/2$ conformally maps the first quadrant onto the lower half-plane, where K being a real constant. Thus, the derivative of the complex potential takes the form:

$$\frac{dw}{d\zeta} = K\zeta. \tag{17}$$

Dividing (17) by (16), we obtain the expression

$$\frac{dz}{d\zeta} = \frac{K\zeta}{v_0}\sqrt{\frac{1+\zeta}{1-\zeta}}\exp\left[-\frac{1}{\pi}\int_0^1 \frac{d\delta_b}{d\xi}\ln\left(\frac{\xi-\zeta}{\xi+\zeta}\right)d\xi + \frac{i}{\pi}\int_0^\infty \frac{d\ln v}{d\eta}\ln\left(\frac{i\eta-\zeta}{i\eta+\zeta}\right)d\eta + i\beta_0\right], \tag{18}$$

whose integration in equation (10) yields the function $z(\zeta)$, which conformally maps the first quadrant of the parameter plane onto the flow region in the z-plane. The integration along the imaginary axis of the parameter region provides the representation of the free streamline. The parameter K and the functions $\delta_b(\xi)$ and $v(\eta)$ are determined from the boundary conditions and physical considerations.

The spatial coordinate along the free surface, $s = s(\eta)$, and along the wetted part of the cylinder, $s_b = s_b(\xi)$, is determined as follows:

$$s(\eta) = -\int_0^\eta \left|\frac{dz}{d\zeta}\right|_{\zeta=i\eta'} d\eta' = -\int_0^\eta \frac{1}{v(\eta')}\left|\frac{dw}{d\zeta}\right|_{\zeta=i\eta'} d\eta' = -K\int_0^\eta \frac{\eta'}{v(\eta')}d\eta', \tag{19}$$

$$s_b(\xi) = \int_0^\xi \frac{ds_b}{d\xi'}d\xi', \qquad \frac{ds_b}{d\xi} = \left|\frac{dz}{d\zeta}\right|_{\zeta=\xi}. \tag{2.20–2.21}$$

The real factor K is determined from the condition for the length of the wetted part of the cylinder, s_w. By substituting (18) into (2.21) and using (2.20), we obtain:

$$s_w = \frac{K}{v_0}\int_0^1 \xi\sqrt{\left|\frac{1+\xi}{1-\xi}\right|} \times \exp\left[-\frac{1}{\pi}\int_0^1 \frac{d\delta_b}{d\xi'}\ln\left|\frac{\xi'-\xi}{\xi'+\xi}\right|d\xi' - \frac{1}{\pi}\int_0^\infty \frac{d\ln v}{d\eta}\left(\pi - 2\tan^{-1}\frac{\eta}{\xi}\right)d\eta\right]d\xi. \tag{22}$$

2.2 Integro-differential equations in the functions $\delta_b(\xi)$ and $v(\eta)$

The body shape is defined by the slope, $\delta_b = \delta_b(s_b)$. By making the change of variables $s_b = s_b(\xi)$ and utilizing (2.21), we derive the following integro-differential equation for the function $\delta_b(\xi)$:

$$\frac{d\delta_b}{d\xi} = \frac{d\delta_b}{ds_b}\frac{ds_b}{d\xi} = \frac{d\delta_b}{ds_b}\frac{K\xi}{v_0}\sqrt{\left|\frac{1+\xi}{1-\xi}\right|} \times \exp\left[-\frac{1}{\pi}\int_0^1 \frac{d\delta_b}{d\xi'}\ln\left|\frac{\xi'-\xi}{\xi'+\xi}\right|d\xi' - \frac{1}{\pi}\int_0^\infty \frac{d\ln v}{d\eta}\left(\pi - 2\tan^{-1}\frac{\eta}{\xi}\right)d\eta\right]. \tag{23}$$

where $d\delta_b/d\xi$ appears on both the left and right-hand sides, allowing it to be solved using the method of successive approximations.

To derive an integral equation for the function $v(\eta)$, we first need to obtain an expression for the curvature κ along the free boundary, specifically along the imaginary axis η of the parameter region. The slope of the free surface is determined from

equation (18) as follows:

$$\theta(\eta) = \arg\left(\frac{dz}{d\zeta}d\zeta\right)_{\zeta=i\eta}$$
$$= \tan^{-1}\eta + \frac{2}{\pi}\int_0^1 \frac{d\delta_b}{d\xi}\tan^{-1}\frac{\eta}{\xi}d\xi + \frac{1}{\pi}\int_0^\infty \frac{d\ln v}{d\eta'}\ln\left|\frac{\eta'-\eta}{\eta'+\eta}\right|d\eta' + \beta_0 + \pi. \quad (24)$$

Differentiating the above equation and considering equation (19), we find the curvature of the free surface as follows:

$$\kappa(\eta) = \frac{d\theta}{ds} = \frac{\frac{d\theta}{d\eta}}{\frac{ds}{d\eta}} = -\frac{v(\eta)}{K\eta}\left(\frac{1}{1+\eta^2} + \frac{2}{\pi}\int_0^1 \frac{d\delta_b}{d\xi}\frac{\xi d\xi}{\xi^2+\eta^2} - \frac{2}{\pi}\int_0^\infty \frac{d\ln v}{d\eta'}\frac{\eta' d\eta'}{\eta'^2-\eta^2}\right). \quad (25)$$

It should be noted that the equation for the curvature has two singular points: one at the point of flow detachment, $\eta = 0$, and another at infinity, arising from the infinite limit of integration in the second integral.

By substituting equation (25) into the dynamic boundary condition (7), we obtain the following singular integral equation in the function $d\ln v/d\eta$

$$\frac{1}{\eta}\left(\frac{2}{\pi}\int_0^\infty \frac{d\ln v}{d\eta'}\frac{\eta' d\eta'}{\eta'^2-\eta^2} - \frac{1}{1+\eta^2} - \frac{2}{\pi}\int_0^1 \frac{d\delta_b}{d\xi}\frac{\xi d\xi}{\xi^2+\eta^2}\right) = \frac{\mathrm{We}\cdot K}{2v(\eta)}(1-v^2), \quad (26)$$

where $v(\eta) = v_0 \exp\left(\int_0^\eta \frac{d\ln v}{d\eta'}d\eta'\right)$ and $v_0 = \sqrt{1+2/(r\mathrm{We})}$. The solution to the above singular integral equation requires special treatment. Instead of solving the equation with respect to the function $d\ln v/d\eta$, we will use the boundary condition (7) to derive a system of nonlinear equations concerning the velocity magnitudes at specific nodes on the free surface. This will be discussed further in Section 3.2.

2.3 Condition for flow detachment

The Brillouin-Villat criterion ([4, 19]) was developed for free-streamline detachment without considering surface tension. However, since the criterion has a geometric nature — stating that the free-streamline should not cross the body — it can also be applied to determine the free-streamline detachment in the presence of non-zero surface tension. Specifically, this means that

$$\lim_{s_b\to 0}\frac{d\ln v_b}{ds_b} = \lim_{\xi\to 0}\frac{\frac{d\ln v_b}{d\xi}}{\frac{ds}{d\xi}} = 0, \quad (27)$$

where s_b is the arc length coordinate on the body, $\zeta = \xi$. By taking the derivative of the magnitude of the complex velocity (16) with $\zeta = \xi$

$$\ln v_b(\xi) = \ln \left| \frac{dw}{dz} \right|_{\zeta=\xi} = \ln \left[v_0 \sqrt{\left| \frac{1-\zeta}{1+\zeta} \right|} \right] + \frac{1}{\pi} \int_0^1 \frac{d\delta_b}{d\xi'} \ln \left| \frac{\xi' - \xi}{\xi' + \xi} \right| d\xi' + \frac{1}{\pi} \int_0^\infty \frac{d \ln v}{d\eta} \left(\pi - 2 \tan^{-1} \frac{\eta}{\xi} \right) d\eta, \tag{28}$$

differentiating it with respect to ξ and using (2.21) for the derivative of the arc length coordinate, we obtain:

$$\lim_{\xi \to 0} \frac{d \ln v_b / d\xi}{ds_b / d\xi} = \lim_{\xi \to 0} \frac{v(\xi)}{K\xi} \left[\frac{-1}{1-\xi^2} + \frac{1}{\pi} \int_0^1 \frac{d\delta_b}{d\xi'} \frac{-2\xi' d\xi'}{\xi'^2 - \xi^2} + \frac{1}{\pi} \int_0^\infty \frac{d \ln v}{d\eta} \frac{2\eta d\eta}{\eta^2 + \xi^2} \right]. \tag{29}$$

The denominator is singular as $\xi \to 0$. Therefore, the numerator must be equal to zero, or

$$\int_0^1 \frac{d\delta_b}{d\xi} \frac{d\xi}{\xi} - \int_0^\infty \frac{d \ln v}{d\eta} \frac{d\eta}{\eta} + \frac{\pi}{2} = 0. \tag{30}$$

This equation is in terms of the unknown length of the wetted part of the body, s_w, which influences the function $\delta_b(\xi) = \delta_b[s_b(\xi)]$, $0 < s_b(\xi) < s_w$, $0 \le \xi \le 1$.

The initial boundary-value problem (1) - (6) has been reduced to a sytem of non-linear equations (22) and (30) for the unknowns K and S_w, along with two integral equations (23) and (26) for the unknown functions $\delta_b(\xi)$ and $v(\eta)$. which are solved throughout the numerical method shown in the following section.

3 Numerical method

3.1 Distribution of nodes

The solution is sought in discrete form on a fixed set of points ξ_j, for $j = 1, \ldots, M$, along the real axis of the parameter region, and a fixed set of points η_i for $i = 1, \ldots, N$ along its imaginary axis. The total number of points N is selected in the range of 200 to 1600, while M is chosen in the range of 400 to 1000 to verify the convergence of the solution procedure. The points ξ_j are distributed to achieve a higher density of nodes $s_{bj} = s_{bj}(\xi_j)$ at points O and A, where the solution exhibits singularities. Within the interval $[0, \xi_{M/2}]$, the points are arranged as a geometric series:

$$\xi_j = \xi_1 + \xi_2 \frac{q^{j-1} - 1}{q - 1}, \quad j = 3, \ldots, M/2, \tag{31}$$

where $\xi_1 = 10^{-9}$, $\xi_2 = 10^{-6}$, and q is determined by the condition that $\xi_{M/2} = 0.3$. In the interval $[\xi_{M/2}, 1]$, the points ξ_j are distributed as

$$\xi_j = \xi_{M/2} + (1 - \xi_{M/2}) \sin \left[\pi \frac{(j - M/2)}{M} \right], \quad j = M/2 + 1, \ldots, M. \tag{32}$$

This distribution ensures a denser node allocation in regions of interest, facilitating accurate representation of the flow characteristics.

The distribution of the nodes η_i is selected to provide a higher density of points for the potential $\phi_i = K\eta_i^2/2$ on the free surface, particularly near the flow detachment point O. In contrast, a uniform distribution of ϕ_i is maintained along the remainder of the free surface:

$$\eta_i = \eta_1 + (\eta^T - \eta_1)\left\{1 - \cos\left[\frac{\pi}{2}\frac{i-1+j_0}{N-1+j_0}\right]\right\}^{\frac{1}{2}}, \quad i = 2, \ldots, N. \tag{33}$$

where $\eta_1 = 10^{-6}$. The index $j_0 = 5$ ensures that the length of the interval remains smaller than the distance from the singular point $\eta_1 = 0$, specifically, $\Delta\eta_j \ll \eta_2 - \eta_1$ for $j = 3, 4, \ldots, N$. The point $\eta_N = \eta^T$ denotes where the integrals along the imaginary axis are truncated. The impact of this truncation will be analyzed in subsequent sections. The distribution $s_i = s(\eta_i)$ will be influenced by both the potential points ϕ_i and the velocity magnitude $v(\eta)$ on the free surface, governed by the relationship $ds = d\phi/v(\eta)$.

The integrals appearing in Eq. (14) are evaluated analytically using linear interpolation of the functions $\delta_b(\xi)$ on the intervals (ξ_{j-1}, ξ_j), and the function $\ln v(\eta)$ on the intervals (η_{i-1}, η_i):

$$\frac{1}{\pi}\int_{\xi_{j-1}}^{\xi_j} \frac{d\delta_b}{d\xi} \ln\left(\frac{\xi-\zeta}{\xi+\zeta}\right) d\xi = \Delta\delta_{bj} A_j(\xi_{j-1}, \xi_j, \zeta), \quad j = 2, ..., M \tag{34}$$

$$\frac{1}{\pi}\int_{\eta_{i-1}}^{\eta_i} \frac{d\ln v}{d\eta} \ln\left(\frac{i\eta-\zeta}{i\eta+\zeta}\right) d\xi = \Delta(\ln v)_i A_i(\eta_{i-1}, \eta_i, \zeta/i), \quad i = 2, ..., N \tag{35}$$

where

$$\Delta\delta_{bj} = \delta_b(\xi_j) - \delta_b(\xi_{j-1}), \quad \Delta(\ln v)_i = \ln\frac{v_i}{v_{i-1}},$$
$$A_j(\xi_{j-1}, \xi_j, \zeta) = \frac{1}{\pi\Delta\xi_j}\int_{\xi_{j-1}}^{\xi_j} \ln\left(\frac{\xi-\zeta}{\xi+\zeta}\right) d\xi,$$

The integral in the above equation is evaluated analytically, and the result is the nonsingular functions $A_j(\xi_{j-1}, \xi_j, \zeta)$.

3.2 Numerical solution of the singular integral equation

We use Newton's method to solve the singular integral equation (26) at the collocation points $\bar{\eta}_i$, where $i = 2k$, $k = 1, 2, , ..., \bar{K}$, $\bar{K} = N/2$, and $\bar{\eta}_i = q\eta_i + (1-q)\eta_{i-1}$. The parameter q is chosen within the interval $0 < q < 1$. By applying linear interpolation for the functions $\delta_b(\xi)$ and the function $\ln v(\eta)$ in the integrals appearing in (26), we

obtain a system of nonlinear equations for the unknown velocity values $v_{2k} = v(\eta_{2k})$:

$$\frac{1}{\pi}\sum_{k=1}^{\bar{K}}\left[\ln\frac{v_{2k}}{v'_{2k-1}}F_{2k}(\bar{\eta}_{2k}) + \ln\frac{v'_{2k-1}}{v_{2k-2}}F_{2k-1}(\bar{\eta}_{2k})\right] - \frac{1}{\pi}\sum_{j=1}^{M}\frac{\Delta\delta_{bj}}{\Delta\xi_j}\ln\frac{\xi_j^2+\bar{\eta}_{2k}^2}{\xi_{j-1}^2+\bar{\eta}_{2k}^2}$$
$$= \frac{\mathrm{We}K\bar{\eta}_{2k}}{2v_{2k}}\left(1-v_{2k}^2\right) + \frac{1}{1+\bar{\eta}_{2k}^2}, \qquad k = 1,\ldots,\bar{K}. \tag{36}$$

The velocities v'_{2k-1} at the nodes η_{2k-1} are determined using linear interpolation of the set of magnitudes v_{2k}:

$$v'_{2k-1} = \frac{\eta_{2k}-\eta_{2k-1}}{\eta_{2k}-\eta_{2k-2}}v_{2k-2} + \frac{\eta_{2k-1}-\eta_{2k-2}}{\eta_{2k}-\eta_{2k-2}}v_{2k},$$

and

$$F_{2k}(\bar{\eta}_{2k}) = \frac{1}{\eta_{2k}-\eta_{2k-1}}\ln\frac{\eta_{2k}^2-\bar{\eta}_{2k}^2}{\eta_{2k-1}^2-\bar{\eta}_{2k}^2}$$

The Jacobian of the system (36) is evaluated numerically using the central difference with $\Delta v_{2k} = 10^{-8}$.

At each iteration, integro-differential equation (23) is solved using the method of successive approximations, which in the discrete form becomes

$$\frac{(\Delta\delta_{bj})^{\{m+1\}}}{\Delta\xi_j} = \frac{\delta_b[s_b^{\{m\}}(\xi_j)] - \delta_b[s^{\{m\}}(\xi_{j-1})]}{\xi_j - \xi_{j-1}}, \tag{37}$$

where the arc length along the body, $s_{bj}^{\{m\}} = s_b^{\{m\}}(\xi_j)$ is evaluated using (2.20–2.21) with $(\Delta\delta_b)_j^{\{m\}}/\Delta\xi_j$ known at the m iteration. The iteration process converges very fast. After 5 to 10 iterations the error is below a prescribed tolerance of 10^{-6}.

The system of equations features two singular points: one at $\eta = 0$ and another at $\eta = \infty$. Consequently, it is essential to investigate the influence of node distribution near $\eta = 0$ and the effect of truncating the integral in equation (26) at some point η^T:

$$\frac{2}{\pi}\int_0^{\infty}\frac{d\ln v}{d\eta'}\frac{\eta' d\eta'}{\eta'^2-\bar{\eta}_k^2} = \frac{1}{\pi}\int_0^{\eta^T}\frac{d\ln v}{d\eta'}\frac{2\eta' d\eta'}{\eta'^2-\bar{\eta}_k^2} + Er(\eta,\eta^T), \tag{38}$$

where $Er(\eta,\eta^T)$ denotes the error.

Since the free surface has a wave-like profile, both the curvature and the velocity magnitude at the free boundary vary periodically in accordance with equation (7). The velocity reaches unity only at the inflection points, where the curvature becomes zero. By truncating the computational domain at one of these inflection points, the impact of the truncation on the flow parameters and on the detachment angle is minimized, because downstream of point T the velocity remains equal to 1. Thus, there is an issue to determine such a point η^{T*} for which the error $Er(0,\eta^{T*})$ at the detachment point disappears. It is described in the following sections 3.3 and 3.4..

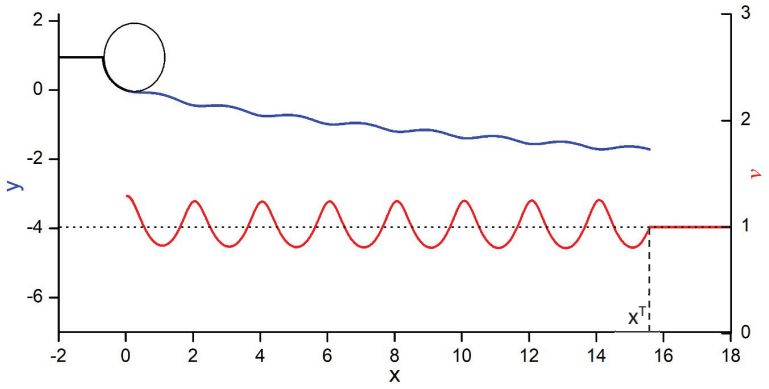


Fig. 2 The free surface shape (left axis, blue line) and the velocity magnitude along the free surface (right axis) for a Weber number of We = 3 and truncation parameter $\eta^T = 3.89$.

3.3 Truncation issue

To estimate $Er(\eta, \eta^T)$ at least at the point $\eta = 0$, we utilize the Brillouin-Villat condition (27) in the physical plane instead of its form (30) in the parameter plane, applying it to the arc length coordinate on the free surface as it approaches the detachment point. This approach is valid due to the continuity of both the velocity magnitude and its derivative at the detachment point,

$$\lim_{s \to 0} \frac{d \ln v}{ds} = 0. \tag{39}$$

In discrete form, the above equation is expressed as:

$$v_0 - v_2 = 0, \tag{40}$$

where $v_0 = \sqrt{1 + 2/(r\mathrm{We})}$; v_2 is the velocity magnitude at the node $\bar{\eta}_1 = \eta_2$, the nearest node to the detachment point. The velocity v_2 is obtained from the solution of the system of nonlinear equations (36).

Figure 2 illustrates the typical shape of the free surface and the velocity magnitude along it. The velocity at the detachment point, v_0, is greater than the velocity at infinity due to the curvature of the body and the surface tension. This difference creates an initial perturbation on the free surface, which propagates downstream and leads to the formation of a wavy surface profile.

At the truncation point, the velocity is given by

$$v^T = v(\eta^T) = 1. \tag{41}$$

This condition at infinity holds for any value of η^T. However, since η^T is finite, truncation introduces errors in the computations of the parameters K, γ, and other flow parameters.

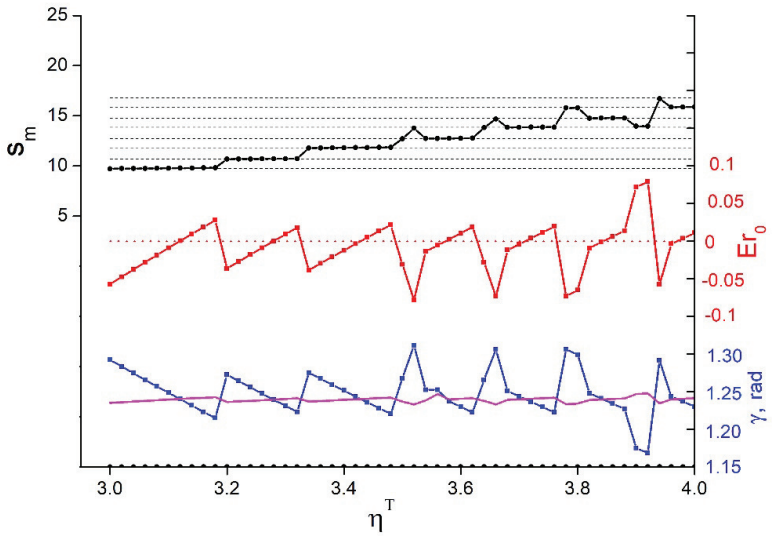


Fig. 3 The arc length of the free surface, $s_m(\eta^T)$ (black line with symbols) , the error in the computation of the integral (38), Er_0 (red line), and the detachment angle γ (blue line), along with the sum $\gamma + Er_0$ (magenta line) for Weber number We = 3. The solid circles indicate the computed values.

In figure 3, the arc length of the free surface $s_m = s(\eta^T)$, the angle of detachment γ, and the error in the detachment condition, (30) due to truncation $Er_0(\eta^T) = Er(0, \eta^T)$, are plotted against the truncation parameter η^T for Weber number We = 3. It is observed that the arc length $s_m(\eta^T)$ exhibits step changes, despite the expectation of a continuous dependence as described by (19). Furthermore, the magnitude of these step changes is about half the wavelength $\Delta s_m \approx \lambda/2 = 1.036$ (see Table 2 for We = 3), fulfilling the condition (41), such that the total length s_m accommodates an integer number of half-waves. This observation is consistent with the results presented in figure 2. When s_m remains constant, a small variation in η^T leads to a minor adjustment in both the angle of detachment γ and the error Er in equation (38). From figure 3, it is evident that the error oscillates around zero. This indicates the presence of points η^{*T} for which error becomes zero, or

$$Er(0, \eta^{*T}) = 0. \tag{42}$$

3.4 Convergence of the solution

The solution of the problem exhibits two singularities, as indicated in the equation for the curvature (25). These singularities can significantly influence the results, particularly the angle of flow detachment γ and the shape of the free surface. Therefore, it is imperative to analyze the effects of truncation and the mesh distribution on the computed parameters. In Table 1, we present the values of the detachment angle γ for various node distributions N. The number of nodes along the real axis was fixed

$N = 200$			$N = 400$			$N = 800$			$N = 1600$		
η_2	η^{*T}	γ	η_2	η^{*T}	γ	η_2	η^{*T}	γ	η_2	η^{*T}	γ
0.0925	3.104	70.886	0.0471	3.122	71.030	0.0238	3.134	71.051	0.0120	3.141	71.040
0.1016	3.408	70.838	0.0518	3.433	71.014	0.0262	3.448	71.044	0.0132	3.456	71.036
0.1205	4.044	70.702	0.0580	3.848	70.967	0.0294	3.870	71.011	0.0148	3.881	71.007
0.1303	4.374	70.667	0.0636	4.216	70.976	0.0331	4.364	71.012	0.0167	4.381	71.012
0.1521	5.105	70.519	0.0733	4.858	70.942	0.0380	5.011	71.010	0.0192	5.035	71.017

Table 1 Angle of flow detachment at the contact point O with surface tension for Weber number We = 3.

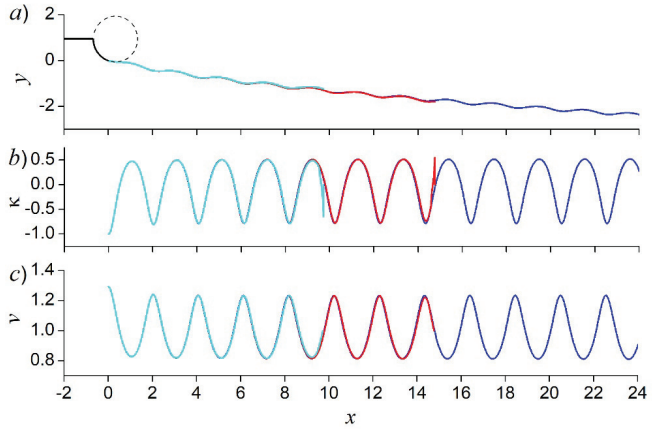


Fig. 4 Free-surface flow for Weber number We = 3 and various truncation values:$\eta^{*T} = 3.14$ (cyan); 3.88 (red); 5.04 (blue). *a*) shape, *b*) curvature, *c*) velocity magnitude.

at $M = 400$. To ensure accurate representation near the singular point $\xi = 0$, the nodes were distributed as a geometric series, with the first node set at $\xi_2 = 10^{-5}$. The nodes corresponding to the cylinder surface were selected such that $s_j \sim \xi_j^2$. This choice, combined with the specified distributions in equations (32) and (33), ensures that the integrals along the real axis over the interval $(0, 1)$ are calculated with sufficient precision. The initial values of the truncation parameter was chosen in the range $3.0 < \eta^T < 5.0$. The final values η^{*T}, which satisfy equation (42), are also shown in Table 1.

The results presented in the columns correspond to different values of the truncation parameter η^{*T} and varying distances between the singular point $\eta = 0$ and the nearest node η_2. The columns reflect different numbers of nodes on the free surface, indicating how the discretization impacts the computed detachment angle γ. The results in the table show the robustness of the angle of flow detachment γ against variations in the truncation point η^{*T} and the proximity of the nearest node η_2 to the singular point. This observation is significant, indicating that the numerical method yields consistent results for the angle of detachment regardless the truncation of the integrals.

The effects of truncation and node distribution are illustrated in figure 4, showcasing the free surface shape, curvature, and velocity magnitude along the free surface. Notably, the computational accuracy is sufficiently high, as evidenced by the overlapping curves for larger truncation values (blue) and smallest values (cyan). Both the curvature and velocity magnitude exhibit oscillations along the free surface.

The amplitude of these oscillations remains constant downstream, indicating a stable wave pattern. At the detachment point, the velocity acts as an initial perturbation that propagates downstream, resulting in the observed waving of the free surface. Importantly, at the detachment point, the curvature is equal to -1, matching the curvature of the cylinder. Towards the end of the computational region the effects of truncation on the free surface and curvature are minimal, remaining consistent within half of the wavelength. This suggests that the influence of truncation diminishes as one moves downstream, highlighting the robustness of the numerical method employed.

3.5 Effect of curvature correction

Yoon and Semenov [37] assumed that the curvature magnitude decreases monotonically. Starting from the detachment point, where the curvature equals that of the body, it decreases either to zero at infinity (for an infinite cavity) or to a minimum at the point where the free surface meets the solid boundary enclosing the cavity. This assumption enabled the use of the method of successive approximations and yielded a convergent solution. This assumption aligns with previous research suggesting that the free surface has a wave-free shape. In a discrete form, this assumption can be expressed as:

$$|\kappa_i| < |\kappa_{i-1}|, \qquad i = 2, \ldots, N. \tag{43}$$

To solve the system of equations, the boundary condition (7) was applied directly, replacing Equation (26). The method of successive approximation was employed to solve the equations (7), (23), (26), and (30). The results showed that the constraint (43) influenced curvature only within a limited region near the detachment point, approximately half of the wavelength in the present calculations. Beyond this region, the curvature magnitude decreased progressively along the free surface. Thus, the curvature correction near the detachment point resulted in the wave-free free-surface downstream.

The computed free-surface contours from this study are compared in figure 5 with the results presented in figure 2a of [37]. It is seen that the dashed lines are positioned within the waving free surfaces obtained in the present study.

The effect of surface tension on free-streamline flows has been examined by many authors (see, e.g., [1, 2, 33–35]). Using matched asymptotic expansions, Ackerberg [1] analyzed classical potential flow near a sharp trailing edge with small capillary forces. His local solution regularizes the curvature and pressure-gradient singularities of the classical inviscid model and predicts a stationary capillary wave along the free streamline. In contrast, in papers [33–35] the capillary waves are not computed, because singular behavior of the velocity and pressure at the detachment point is assumed. Also, those studies determine the unknown surface-velocity magnitude via Brodetsky's series-truncation method, which is effective for monotonic profiles but

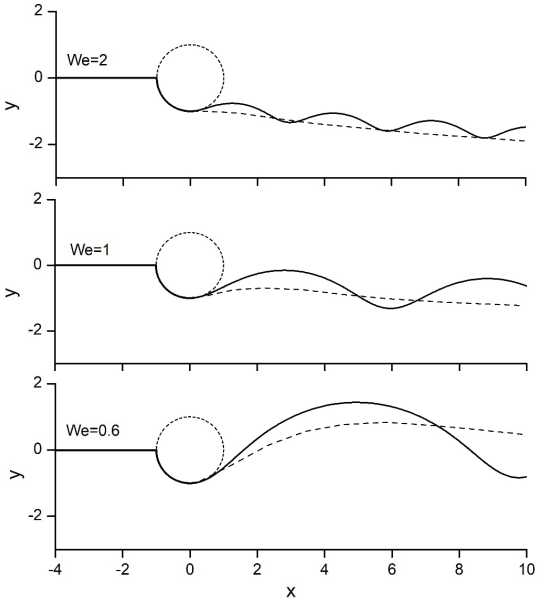


Fig. 5 Comparison of the free-surface contours drown in the system of coordinate with the origin at the center of the cylinder: present computations (solid lines); results [37] (dashed lines).

poorly conditioned for periodic ones, as accurately capturing oscillations requires a large number of coefficients.

4 Results and discussion

4.1 Circular cylinder

The lower part of the flow past a circular cylinder is shown in figure 6 for various We numbers, including the case for We $= \infty$, corresponding to zero surface tension. The predicted detachment angle for this case is $\gamma = 55.04°$ (see Table 2 below), which matches the known value [19]. For We $= \infty$, the slope of the free surface decreases monotonically from γ at the detachment point to zero at infinity. In this case, the velocity magnitude along the entire free surface, including the detachment point, remains constant, $v(\eta) \equiv v_\infty = 1$.

When We $< \infty$, the free surface exhibits capillary waves, with both the wavelength and amplitude increasing as surface tension increases. The truncation region TO, where the velocity remains constant and equals the velocity at infinity, is not shown in figure 6. In the figure, a dashed line crosses the free surface at points where the velocity equals 1, while a dotted line represents the flow's axis of symmetry.

It can be seen that the intervals below the dashed line, where the velocity magnitude $v > 1$, are shorter than those above the line, where $v < 1$. This characteristic of capillary waves was revealed by Crapper [7]. For We $= 1$, the slope of the dashed line starts off negative but gradually approaches zero at infinity. At We $= 0.6$, the slope

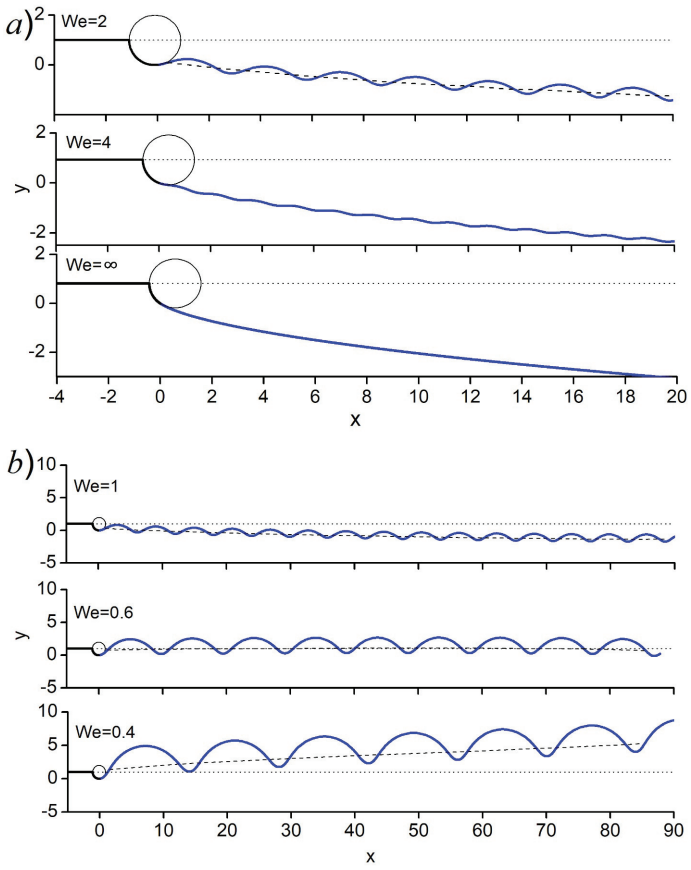


Fig. 6 Free surface shapes for various Weber numbers, with values indicated in the figure.

is nearly zero from the outset. At We = 0.4, the slope of the dashed line becomes positive but also gradually tends to zero at infinity.

In figure 7 are compared one period of the wave pattern for the progressive capillary waves on the cavity surface at $We = 0.6$ and the Crapper's wave pattern [7] on the surface of infinite depth fluid. In both cases the surface tension is balanced by liquid inertia only. They both corresponds to progressive waves in the freestream frame of reference but were obtained in the translating frame of reference within the steady formulation of the problem. The free-surface profiles coincide almost everywhere; the slight discrepancy on the right-hand side is likely due to the limited fidelity of the original figure in [7].

For We = 1, the first wave crest almost touches the flow symmetry axis (dotted line). As We decreases to 0.6, the wavelength and amplitude increase further, causing the free surface to cross the symmetry line. This situation is physically impossible for flow around a cylinder because the upper and lower free streamlines would collide

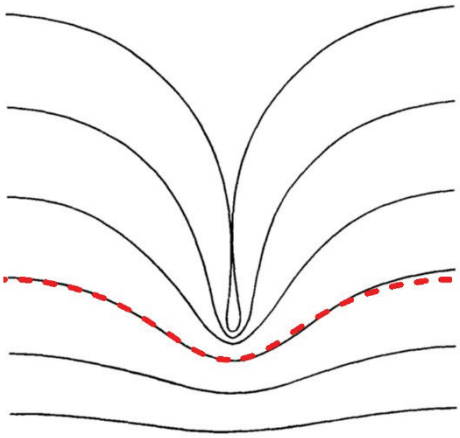


Fig. 7 Comparison of the wave profile in figure 6 at We = 0.6 (red dashed line) with the Crapper's solution [7]. Our profile is scaled to match Crapper's wavelength.

behind the cylinder. However, such a situation could be applicable to the case of a semi-infinite solid plate with a rounded trailing edge.

The pressure coefficient on the cylinder surface, c_{pb}, is derived from the Bernoulli equation as follows:

$$c_{pb} = \frac{2(p - p_\infty)}{\rho U^2} = 1 - \left.\frac{dw}{dz}\overline{\frac{dw}{dz}}\right|_{\zeta=\xi}. \tag{44}$$

At the detachment point, the dimensionless curvature takes the value $\kappa = -1$, and the pressure coefficient at point O, $c_{pO} = -2/\mathrm{We}$.

The pressure distribution along the wetted portion of the cylinder is illustrated in figure 8 for various Weber numbers. It is evident that as the Weber number decreases, the magnitude of the negative pressure at the detachment point increases, leading to a larger region of the cylinder experiencing negative pressure. This behavior affects the drag coefficient C_D, which is presented in Table 1. The drag coefficient of the cylinder is calculated using the following formula:

$$C_D = \frac{4D}{\rho U^2\, 2H} = -\frac{2}{\rho U^2 H}\int_0^{s_A} (p - p_\infty)(\mathbf{n}\cdot\mathbf{i})\, dS = \Re\left\{-i\int_0^1 \left(1 - \frac{dw}{dz}\overline{\frac{dw}{dz}}\right)\frac{dz}{d\xi}\, d\xi\right\}, \tag{45}$$

where D is the drag of the lower part of the cylinder, and $\mathbf{i}$ is the unit vector in the x-direction. The formula (45) accounts for the total drag on both the upper and lower part of the cylinder by exploiting the up-down symmetry of the problem. The integration in the second integral is performed along the interval $[0, 1]$ on the real axis of the first quadrant in the parameter plane.

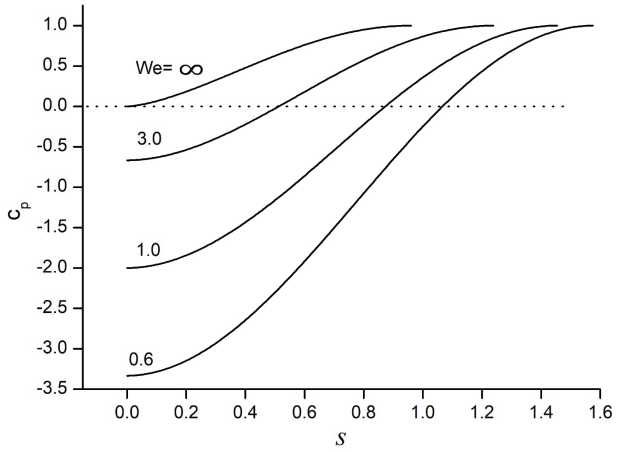


Fig. 8 Pressure coefficient along the wetted part of the cylinder for various Weber numbers. The point $s = 0$ corresponds to the detachment point where $c_p = c_{pO}$, and the end of the curves corresponds to the stagnation point A, where $c_p = 1$.

The drag coefficient decreases as the Weber number decreases and even becomes negative for Weber numbers We < 1.14. This means that a pulling force appears instead of a drag force. It occurs due to the fact that a large part of the wetted cylinder surface experiences a pressure that is lower than that on the unwetted rear part of the cylinder, as can be seen in figure 8.

Table 2 presents the values of the main parameters. As the Weber number decreases, the angle of detachment, wavelength, and wave amplitude all increase, along with the amplitudes of the curvature and velocity. For Weber numbers greater than 100, the capillary wave nearly disappears. Although the oscillation of the curvature also diminishes, it does so more slowly than the wave amplitude, as both the wavelength and amplitude decrease simultaneously. The relationship between wavelength and amplitude versus Weber number is shown in figure 9 using a logarithmic scale, where they exhibit an almost linear trend. The distance between wave crests and their amplitudes vary slightly near the cylinder but stabilize to a constant value further away.

It is instructive to compare the wavelengths based on the present nonlinear theory and the linear theory of the capillary waves. According to the linear theory the wavelength of the capillary waves is determined by formula [24]

$$\frac{\lambda}{H} = \frac{2\pi}{We}. \tag{46}$$

The wavelength based on the linear theory as well as the ratio $2A_y/\lambda$ showing the steepness of the waves are shown in the table. As one can see, when the steepness $2A_y/\lambda$ is small, formula (46) gives rather accurate agreement. For larger steepness, the nonlinear effects becomes stronger, the agreement between the linear and nonlinear

We	γ	C_D	λ	λ_{lin}	$2A_Y/\lambda$	$2A_Y$	$2A_C$	$2A_V$
∞	55.04	0.4986	-	-	-	0	0	0
100	56.21	0.4958	0.061	0.063	0.0041	0.00025	0.474	0.005
50	57.11	0.4926	0.119	0.126	0.0052	0.00062	0.600	0.013
20	59.32	0.4814	0.306	0.314	0.0087	0.00265	0.835	0.042
15	60.38	0.4744	0.413	0.419	0.0111	0.0046	0.925	0.061
10	62.23	0.4592	0.612	0.628	0.0181	0.0111	1.071	0.107
7	64.29	0.4378	0.875	0.898	0.0272	0.0238	1.177	0.166
5	66.65	0.4072	1.230	1.257	0.0398	0.0490	1.221	0.243
4	68.42	0.3789	1.561	1.571	0.0548	0.0856	1.242	0.312
3	71.04	0.3300	2.073	2.094	0.0681	0.1412	1.286	0.421
2	75.11	0.2303	3.103	3.142	0.0986	0.306	1.296	0.614
1.14	81.94	0.0017	5.270	5.512	0.1569	0.827	1.313	1.022
1	83.34	-0.0649	5.955	6.283	0.1731	1.031	1.286	1.123
0.8	86.28	-0.2057	7.441	7.854	0.1982	1.475	1.260	1.311
0.6	90.26	-0.4184	9.749	10.472	0.2402	2.342	1.248	1.606
0.4	95.75	-0.7941	14.016	15.708	0.3075	4.310	1.247	2.140

Table 2 Main reference parameters for various Weber numbers: the angle of detachment, γ; drag coefficient, C_D; wavelength, λ, wavelength based on the linear theory, λ_{lin}, steepness of the wave, $2A_Y/\lambda$, and its amplitude oscillation range, $2A_Y$; the curvature oscillation range, $2A_C$; and the velocity magnitude oscillation range along the free surface, $2A_V$. The row marked ∞ corresponds to the data reported in [19], which coincides with the present calculations.

results become less accurate, although it still quite good. This agreement demonstrates the correctness of the theoretical approach and the high accuracy of the numerical method.

When the pressure in the liquid drops below the vapor pressure (p_v), cavitation starts. If the pressure on the free streamlines behind the cylinder is $p_\infty = p_v$, liquid cavitation will manifest itself on the wetted part of the cylinder's surface before the liquid reaches the detachment point. The present formulation of problem is valid under the condition:

$$p_{\min} \geq p_v, \tag{47}$$

where $p_{\min}$ is the minimum pressure on the wetted part of the cylinder at the detachment point. To satisfy condition (47), the pressure at infinity must be sufficiently large. By introducing the cavitation number:

$$\sigma = \frac{2(p_\infty - p_v)}{\rho U^2}, \tag{48}$$

and considering ((47), the present solution is valid when:

$$\mathrm{We} > \frac{2}{\sigma}. \tag{49}$$

4.2 Flat plate with rounded edges

In the following analysis we investigate the flow detachment from a flat plate with rounded edges. The width of the plate is given by $H = 2(L+R)$, where L is the length

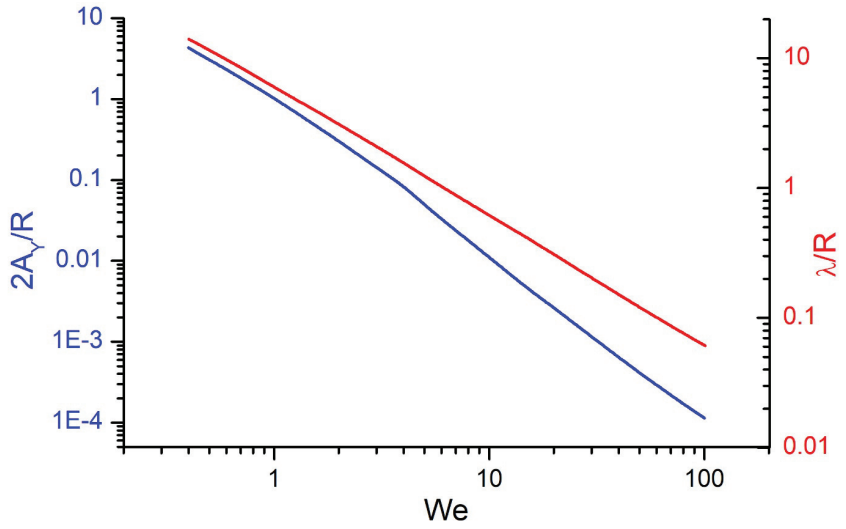


Fig. 9 The wave amplitude (left axis) and the wave length (right axis) versus Weber number.

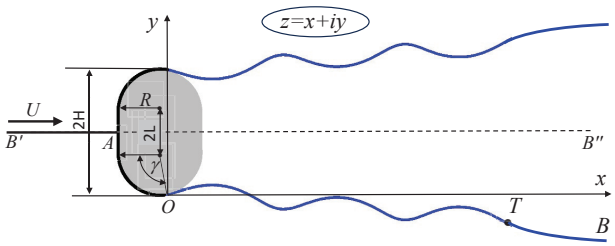


Fig. 10 Sketch of the free-streamline flow past a plate with rounded edges.

of the flat portion, and R is the radius of the rounded edges of the plate. The sketch of the flow is shown in figure 10. The dimensionless radius of the edge is denoted as $r = R/H$. In the special case where the radius r tends to zero, the configuration approaches to a flat plate with sharp edges.

Figure 11 shows the free surface shape (a), curvature (b), and velocity magnitude (c) for various edge radii at Weber number We = 10. For $r = 1$ (circular cylinder), the free surface wave is almost imperceptible, although both the curvature and the velocity magnitude exhibit visible oscillations along the free streamline (blue lines) in panels (b) and (c). As the edge radius decreases, the wave amplitude increases, as seen in figure 11 (a) for $r = 0.2$ and $r = 0.05$. In figure 11(b), the curvature at the detachment point $\kappa = -1/r$, after which the minimum values increase slightly and remain nearly constant. The minimum curvature corresponds to the peaks in velocity magnitude, which are sharper than the troughs. It is important to note that $r = 0.04$ is the smallest radius for which we obtained convergence.

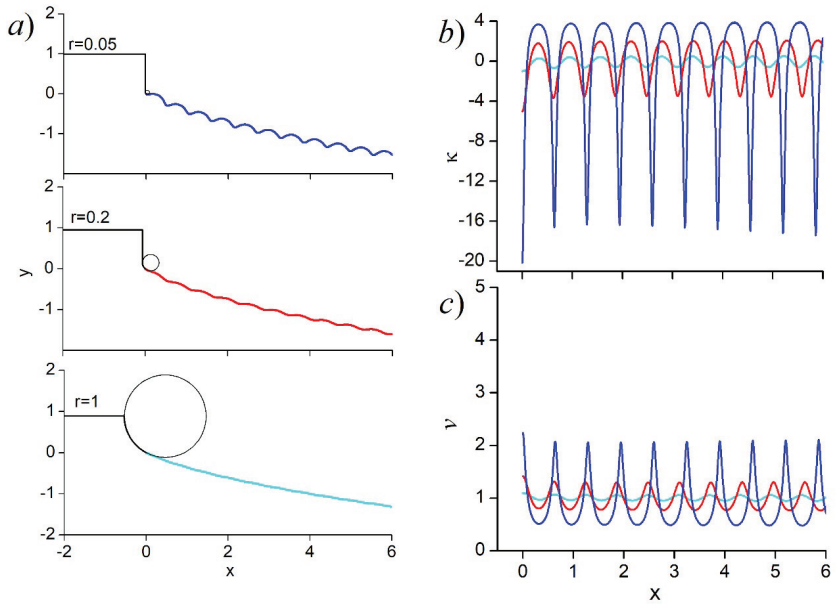


Fig. 11 (a) - flow past a flat plate with the rounded trailing edge for We = 10, (b) - the curvature, and (c) - the velocity magnitude along the free surface for the various edge radiuses: $r = 1$ (blue line), 0.2 (red line), and 0.05 (cyan line).

Similar results are shown in figures 12 and 13 for Weber numbers We = 3 and We = 1, respectively. The wavelength and amplitude are significantly larger compared to We = 10. However, at the same Weber number, the wavelength slightly decreases as the edge radius decreases for both We = 3 and We = 1. This trend is more noticeable in the figure panels (*b*) and (*c*), which depict the behavior of the curvature and velocity magnitude. The dashed line indicates points along the free surface where the velocity equals unity. The portion of the wave above the dashed line corresponds to almost constant positive curvature, or the wave shape largely resembles an arc of circle. At this portion the curvature becomes smaller for the smaller Weber number, and this may have an impact on the convergence of the numerical procedure. The smallest edge radius for which the numerical procedure converges is $r = 0.04, 0.05, 0.12$ for Weber numbers We $= 10, 3, 1$, respectively.

Zhitnikov and Terent'ev [39] (see also [32], p. 151) obtained a cavity shape attached to the plate, which qualitatively resembles those observed here. They noted that complex cavity shapes — sometimes featuring shells with self-intersections — transform into non-self-intersecting free boundaries in cavity flow scenarios. Additionally, at high Weber numbers, the free surface displays very short, small-amplitude capillary waves. The present findings are consistent with their conclusions.

The influence of the plate edge radius on the free-streamline detachment angle and the drag coefficient is illustrated in Figure 14 for various Weber numbers, as indicated in the figure. For We $= \infty$, the angle γ ranges from zero at $r = 0$ to $\gamma = 55.04^\circ$ at $r = 1$, corresponding to the detachment angle for a circular cylinder. Since $v(\eta) \equiv 1$

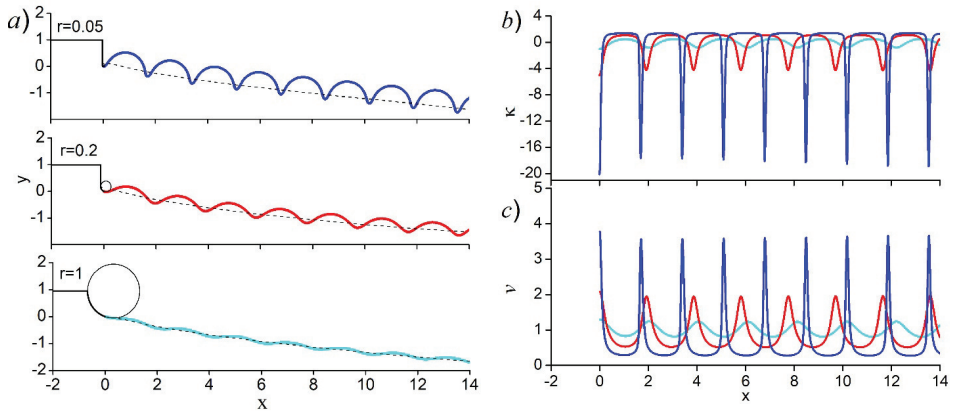


Fig. 12 Same as figure 11, but for Weber number We = 3.

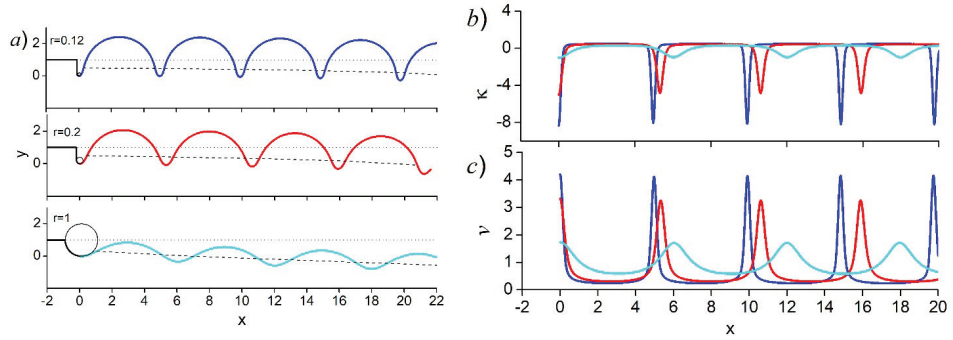


Fig. 13 Same as figure 11, but for Weber number We = 1.

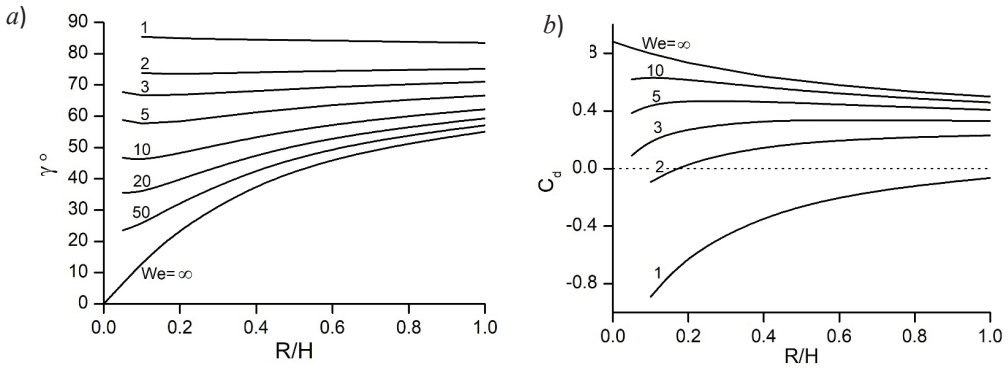


Fig. 14 (a) - the angle of the free-streamline detachment and (b) the drag coefficient versus the edge radius for various Weber numbers indicated in the figures.

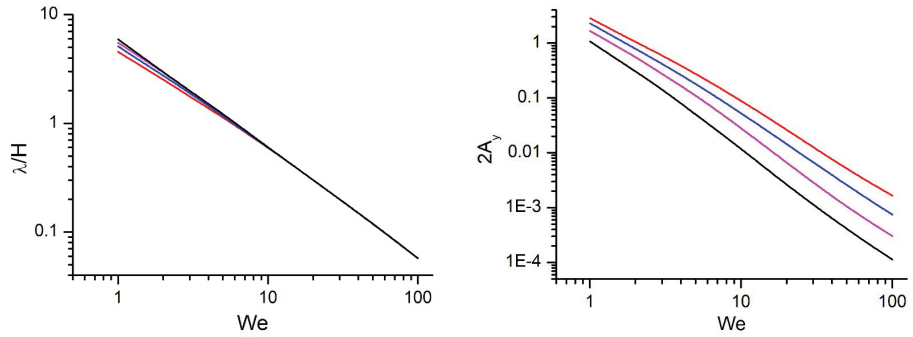


Fig. 15 (a) - the wavelength and (b) the wave amplitude of the free-streamline as fuctions of the Weber number: $r = 1$ (black line); $r = 0.4$ (magenta); $r = 0.2$ (blue line); and $r = 0.1$ (red line).

and $\frac{d \ln v}{d\eta} \equiv 0$, the integrals involving the velocity magnitude vanish in the analysis presented in Section 2. This simplification allows us to obtain results for very small radii of the plate edge, down to $r = 10^{-5}$ in the present calculations. For We $< \infty$, the behavior of the detachment angle γ is significantly influenced by surface tension. In the range $20 <$ We $< \infty$, the angle γ decreases as the edge radius decreases, indicating that inertial forces dominate over surface tension forces for radii in the range $0.05 < r < 1$. For Weber numbers $3 <$ We < 10, the angle γ decreases in the range $0.1 < r < 1$, but then increases for radii down to $r = 0.05$. For We $= 2$, the angle γ remains almost constant in the range $0.1 < r < 1$, suggesting a balance between inertial and surface tension forces for edge radii in this range. For We $= 1$, the angle γ slightly increases in the range $0.1 < r < 1$ indicating that surface tension forces dominate over inertia forces. For smaller edge radii, our numerical procedure does not converge.

For We $= \infty$, the drag coefficient in figure 14(b) varies from $C_D = 0.8798$ for the flat plate ($r = 0$) to $C_D = 0.4986$ for the circular cylinder ($r = 1$). The drag coefficient gets smaller if the Weber number decreases or if the radius of the plate edge decreases. ← **MGB: I don't understand the previous sentence and reworded it, but I'm not sure if I kept the sense you intended?.** This occurs because the velocity at the detachment point, $v_0 = \sqrt{1 + 2/(r\text{We})}$, increases as the product rWe decreases. Consequently, the pressure decreases and can even become negative on the flat front portion of the plate near the plate edge, as predicted by the Bernoulli equation. An exception occurs for relatively larger Weber numbers, We > 5, and radii in the range $0.2 < r < 1$.

The wavelength and the wave amplitude of the free streamline as fuctions of the Weber number are shown in figure 15 for various radii of the plate edge. It is seen in figure 15*a* that the radius of the plate edge weakly affect the wave length. Only for radii $r < 0.4$ and for Weber number We < 10 is the effect of the edge radius visible. We also note that the wavelength exhibits an almost linear dependence in logarithmic coordinates. This suggests extending the analysis to a linear formulation of the problem, assuming small amplitude velocity oscillations along the free streamline. Such an approach could lead to obtaining an analytical dependence $\lambda = \lambda(\text{We})$, similar to the theory of linear free-surface waves.

The wave amplitude also exhibit an almost linear dependence on the Weber number. However, it also depends on the radius of the plate edge. This is consistent with the perturbation of the velocity magnitude at the point point of detachment, $\Delta v = v_0 - 1$, where $v_0 = \sqrt{1 + 2/(r\mathrm{We})}$ depends on the product $r\mathrm{We}$.

5 Conclusions

We have presented a fully nonlinear solution for free streamline flow past a circular cylinder with surface tension. The integral hodograph method was used to derive an expression for the complex velocity in the first quadrant of the parameter region. This expression explicitly includes the velocity magnitude on the free streamline, allowing the original boundary-value problem to be reduced to a system of integral equations. These equations were formulated in terms of the velocity magnitude on the free streamline and the slope of the cylinder surface and were solved numerically using the collocation method.

The position of the free streamline detachment point was determined using the Brillouin-Villat criterion, for which the curvature of the free streamline equals the curvature of the body at the detachment point. Our results showed that the detachment point moves further down along the cylinder as the Weber number decreases.

For the circular cylinder at Weber numbers $\mathrm{We} < 10$, the effect of surface tension manifests as a wave on the free streamline. As the Weber number decreases, both the wavelength and the amplitude of the waves increase. At around $\mathrm{We} \approx 1$, the wave crest grows so large that the lower and upper streamlines intersect. In this case, the physical interpretation of the solution as representing flow past a circular cylinder is no longer valid. However, the solution in this case may be interpreted as representing a flow emerging from a solid plate with a circular trailing edge. The wave profiles on the free streamline closely resemble the solutions obtained by Crapper [7] for travelling capillary waves on fluid of infinite depth. Crapper's class of solutions encompasses overhanging waves, a limiting case where the wave profile entraps a small air bubble, as well as unphysical self-intersecting profiles. For the present problem we did not detect any cases where such overturning or self-intersecting wave profiles are seen.

For a flat plate with rounded edges, the edge radius and surface tension influence the flow detachment angle γ in opposite ways. For smaller edge radii, the inertial force increases due to greater liquid acceleration around the edge, causing the angle γ to decrease. At a Weber number of $\mathrm{We} = 2$, the angle γ remains almost constant for edge radii in the range $0.2 < r < 1$, indicating a balance between inertial and surface tension forces within this range.

Both the plate edge radius and surface tension influence the wave on the free streamline: the smaller the edge radius and Weber number, the larger the wave amplitude of the free streamline. However, the wavelength primarily depends on the Weber number alone. A weak effect of the edge radius on the wavelength is observed only at relatively large wave amplitudes for Weber numbers $\mathrm{We} < 10$.

For both the circular cylinder and the plate with rounded edges, the wavelength exhibits almost linear dependence in the logarithmic coordinates. This suggests

extending the analysis to a linear formulation of the problem, assuming small amplitudes of velocity oscillations along the free streamline. Such an approach could lead to obtaining an analytical dependence $\lambda = \lambda(\mathrm{We})$, similar to the theory of linear free-surface waves.

We found that surface tension reduces the hydrodynamic drag force, which can even become negative. This happens because of the higher velocity, and consequently lower pressure, near the detachment point. This causes the pressure on the wetted front part of the cylinder or on the flat part of the plate with rounded edges to drop below the pressure on the unwetted rear part. We note that the negative drag obtained within the framework of an ideal fluid looks unrealistic for real liquids. The viscosity and wettability of a real liquid affects the flow near to the detachment point. The present formulation of the problem does not account for these effects and their elimination in experiments is a difficult issue. Although we hope that the drag reduction due to surface tension may occur at least for hydrophobic surfaces.

Based on our calculations, we can infer that the present formulation of the problem does not accurately reflect the physics of flow past a flat plate with sharp corner edges for the following reasons: according to equation (7), the velocity at the detachment point tends to infinity for any large but finite Weber number as the cylinder radius $r \to 0$, such that $v_0 = \sqrt{1 + 2/(r\,\mathrm{We})} \to \infty$. Additionally, cavitation may occur before the liquid reaches the edge of the plate. Even with a small but finite edge radius, a steady solution may not exist due to the decreasing curvature — and consequently, a weakening surface tension force — over a larger portion of the wave, which plays a stabilizing role.

Acknowledgements. We are grateful to the anonymous referees for their suggestions which helped us to improve the manuscript. YAS would like to thank the Isaac Newton Institute for Mathematical Sciences, Cambridge, for financial support and hospitality during the programme *The mathematics of multiphase flows with applications*, when work on this paper was undertaken. This work was supported by EPSRC grant EP/V521929/1.

Declarations

- The work of YAS and BN was supported by the National Natural Science Foundation of China (Nos.W2541018, 52521009, 52192693, 52192690, 52371270, 52350410468, and W2433140), to which the authors are most grateful.
- The authors report no conflict of interest

Appendix A Integral formula solving mixed boundary value problem for a complex function.

Let a complex function $F(\zeta)$ defined in the complex plane $\zeta = \xi + i\eta$ and its argument, $\chi(\xi)$, is known on the real axis, and its magnitude, $v(\eta)$, is known on the imaginary

axis, of the first quadrant:

$$\arg\left(F(\zeta)\right) = \chi(\xi), \quad 0 < \xi < \infty, \quad \eta = 0. \tag{A1}$$

$$|F(\zeta)|_{\zeta=i\eta} = v(\eta), \quad 0 < \eta < \infty, \quad \xi = 0. \tag{A2}$$

Then, the following integral formula

$$F(\zeta) = v_\infty \exp\left[-\frac{1}{\pi}\int_\infty^0 \frac{d\chi}{d\xi}\ln\left(\frac{\zeta+\xi}{\zeta-\xi}\right)d\xi - \frac{i}{\pi}\int_0^\infty \frac{d\ln v}{d\eta}\ln\left(\frac{\zeta-i\eta}{\zeta+i\eta}\right)d\eta + i\chi_\infty\right] \tag{A3}$$

recovers the function $F(\zeta)$ in the complex plane ζ such that boundary conditions (A1) and (A2) are satisfied. Here, $v_\infty = \lim_{\eta\to\infty} v(\eta)$ and $\chi_\infty = \lim_{\xi\to\infty}\chi(\xi)$.

Case $\zeta = \xi$.

$$F(\zeta)_{\zeta=\xi} = v_\infty \exp\left[-\frac{1}{\pi}\int_\infty^0 \frac{d\chi}{d\xi'}\ln\left(\frac{\xi+\xi'}{\xi-\xi'}\right)d\xi' - \frac{i}{\pi}\int_0^\infty \frac{d\ln v}{d\eta}\ln\left(\frac{\xi-i\eta}{\xi+i\eta}\right)d\eta + i\chi_\infty\right] \tag{A4}$$

Write the complex logarithm in the first integral in (A4),

$$-\frac{1}{\pi}\int_\infty^0 \frac{d\chi}{d\xi'}\ln\left(\frac{\xi+\xi'}{\xi-\xi'}\right)d\xi' = -\frac{1}{\pi}\int_\infty^0 \frac{d\chi}{d\xi'}\left[\ln\left|\frac{\xi+\xi'}{\xi-\xi'}\right| + i\arg\left(\frac{\xi+\xi'}{\xi-\xi'}\right)\right]d\xi'.$$

Evaluating the integral of the second term,

$$\begin{aligned}
-\frac{1}{\pi}\int_\infty^0 \frac{d\chi}{d\xi'}\arg\left(\frac{\xi+\xi'}{\xi-\xi'}\right)d\xi' &= \frac{1}{\pi}\int_0^\infty \frac{d\chi}{d\xi'}\left[\arg(\xi+\xi') - \arg(\xi-\xi')\right]d\xi' \\
&= -\frac{1}{\pi}\int_0^\infty \frac{d\chi}{d\xi'}\arg(\xi-\xi')\,d\xi' \\
&= -\int_\xi^\infty \frac{d\chi}{d\xi'}\,d\xi' = -\big(\chi(\infty) - \chi(\xi)\big).
\end{aligned}$$

The first integral takes the form:

$$-\frac{1}{\pi}\int_\infty^0 \frac{d\chi}{d\xi'}\ln\left(\frac{\xi+\xi'}{\xi-\xi'}\right)d\xi' = -\frac{1}{\pi}\int_\infty^0 \frac{d\chi}{d\xi'}\ln\left|\frac{\xi+\xi'}{\xi-\xi'}\right|d\xi' - i\big(\chi(\infty) - \chi(\xi)\big).$$

Evaluating the second integral in (A4)

$$\begin{aligned}
-\frac{i}{\pi}\int_0^\infty \frac{d\ln v}{d\eta}\ln\left(\frac{\xi-i\eta}{\xi+i\eta}\right)d\eta &= -\frac{i}{\pi}\int_0^\infty \frac{d\ln v}{d\eta}\left[\ln\left|\tfrac{\xi-i\eta}{\xi+i\eta}\right| + i\arg\left(\tfrac{\xi-i\eta}{\xi+i\eta}\right)\right]d\eta \\
&= -\frac{i}{\pi}\int_0^\infty \frac{d\ln v}{d\eta}\,i\arg\left(\frac{\xi-i\eta}{\xi+i\eta}\right)d\eta \\
&= \frac{1}{\pi}\int_0^\infty \frac{d\ln v}{d\eta}\left(-2\arctan(\eta/\xi)\right)d\eta.
\end{aligned}$$

The integral formula (A3) takes the form

$$F(\zeta)|_{\zeta=\xi} = v_\infty \exp\left[-\frac{1}{\pi}\int_\infty^0 \frac{d\chi}{d\xi'} \ln\left|\frac{\xi+\xi'}{\xi-\xi'}\right| d\xi' + i\,\chi(\xi) - \frac{1}{\pi}\int_0^\infty \frac{d\,\ln v}{d\eta}\left(2\,\arctan(\eta/\xi)\right) d\eta\right]$$

from which it follows that the boundary condition (A1) is satisfied

$$\arg\Big(F(\zeta)|_{\zeta=\xi}\Big) = \chi(\xi).$$

Case $\zeta = i\eta$.

$$F(\zeta)\Big|_{\zeta=i\eta} = v_\infty \exp\left[-\frac{1}{\pi}\int_\infty^0 \frac{d\chi}{d\xi} \ln\left(\frac{i\eta+\xi}{i\eta-\xi}\right) d\xi \;-\; \frac{i}{\pi}\int_0^\infty \frac{d\,\ln v}{d\eta'} \ln\left(\frac{\eta-\eta'}{\eta+\eta'}\right) d\eta' \;+\; i\chi_\infty\right]. \tag{A5}$$

The first integral

$$\begin{aligned}
-\frac{1}{\pi}\int_\infty^0 \frac{d\chi}{d\xi} \ln\left(\frac{i\eta+\xi}{i\eta-\xi}\right) d\xi &= -\frac{1}{\pi}\int_\infty^0 \frac{d\chi}{d\xi}\left[\ln\left|\frac{i\eta+\xi}{i\eta-\xi}\right| + i\,\arg\left(\frac{i\eta+\xi}{i\eta-\xi}\right)\right] d\xi \\
&= -\frac{i}{\pi}\int_\infty^0 \frac{d\chi}{d\xi}\,\arg\left(\frac{i\eta+\xi}{i\eta-\xi}\right) d\xi \\
&= -\frac{i}{\pi}\int_\infty^0 \frac{d\chi}{d\xi}\left(2\arctan(\eta/\xi) - \pi\right) d\xi.
\end{aligned}$$

The second integral

$$\begin{aligned}
-\frac{i}{\pi}\int_0^\infty \frac{d\,\ln v}{d\eta'} \ln\left(\frac{\eta-\eta'}{\eta+\eta'}\right) d\eta' &= -\frac{i}{\pi}\int_0^\infty \frac{d\,\ln v}{d\eta'}\left[\ln\left|\frac{i\eta-i\eta'}{i\eta+i\eta'}\right| + i\,\arg\left(\frac{i\eta-i\eta'}{i\eta+i\eta'}\right)\right] d\eta' \\
&= -\frac{i}{\pi}\int_0^\infty \frac{d\,\ln v}{d\eta'} \ln\left|\frac{i\eta-i\eta'}{i\eta+i\eta'}\right| d\eta' + \frac{1}{\pi}\int_0^\infty \frac{d\,\ln v}{d\eta'}\,\arg\left(\frac{i\eta-i\eta'}{i\eta+i\eta'}\right) d\eta'.
\end{aligned}$$

The argument is evaluated as follows,

$$\arg\left(\frac{i\eta-i\eta'}{i\eta+i\eta'}\right) = \arg(i\eta-i\eta') - \arg(i\eta+i\eta') = \begin{cases} \dfrac{\pi}{2} - \dfrac{\pi}{2} = 0, & 0 < \eta' < \eta, \\ -\dfrac{\pi}{2} - \dfrac{\pi}{2} = -\pi, & \eta < \eta' < \infty. \end{cases}$$

The second term takes the form

$$\frac{1}{\pi}\int_0^\infty \frac{d\,\ln v}{d\eta'}\,\arg\left(\frac{i\eta-i\eta'}{i\eta+i\eta'}\right) d\eta' = \;\frac{1}{\pi}\int_\eta^\infty \frac{d\,\ln v}{d\eta'}\,(-\pi)\,d\eta' = -\ln v(\infty) + \ln v(\eta).$$

Combination of all terms in (A5) yields

$$F(\zeta)\Big|_{\zeta=i\eta} = v_\infty \exp\Bigg[-\frac{i}{\pi}\int_\infty^0 \frac{d\chi}{d\xi}\left(2\arctan(\eta/\xi)-\pi\right)d\xi \\ -\frac{i}{\pi}\int_0^\infty \frac{d\,\ln v}{d\eta'}\,\ln\left|\frac{i\eta-i\eta'}{i\eta+i\eta'}\right|\,d\eta' - \ln v(\infty)+\ln v(\eta)\Bigg].$$

By taking the magnitude of the above equation, it is seen that the boundary condition (A2) is satisfied.

$$\left|F(\zeta)\right|_{\zeta=i\eta} = v(\eta).$$

Appendix B Curvature of the streamline at the point of detachment

In order to evaluate the curvature of the free surface at the detachment point, where at $\eta = 0$ equation (25) has an indeterminate form, we differentiate the numerator and denominator of equation (25) to obtain:

$$\kappa_0 = \lim_{\eta\to 0}\left\{-\frac{1}{K}\frac{dv}{d\eta}\left(\frac{1}{1+\eta^2}+\frac{2}{\pi}\int_0^1\frac{d\delta_b}{d\xi}\frac{\xi\,d\xi}{\xi'^2+\eta^2}-\frac{2}{\pi}\int_0^1\frac{d\,\ln v}{d\eta'}\frac{\eta'\,d\eta'}{\eta'^2-\eta^2}\right)\right\} \\ +\lim_{\eta\to 0}\left\{\frac{2\eta v}{K}\left(\frac{1}{(1+\eta^2)^2}+\frac{2}{\pi}\int_0^1\frac{d\delta_b}{d\xi}\frac{\xi\,d\xi}{(\xi^2+\eta^2)^2}+\frac{2}{\pi}\int_0^1\frac{d\,\ln v}{d\eta'}\frac{\eta'\,d\eta'}{(\eta'^2-\eta^2)^2}\right)\right\} \quad \text{(B6)}$$

The first term in the above equation equals zero due to the flow detachment condition (27). In order to evaluate the second term containing the singular integrals, we have to estimate the behavior of the functions $d\ln v/d\eta$ at $\eta\to 0$ and $d\delta_b/d\xi$. From the Brillouin-Villat condition (27) and continuity of the function $v(s)$ at the detachment point, it follows that

$$\lim_{s\to 0}\frac{d\ln v}{ds} = \lim_{\eta\to 0}\frac{\frac{d\ln v}{ds}}{\frac{ds}{d\eta}} = 0, \quad \text{(B7)}$$

In view of equation (19), it can be seen that for $\eta\to 0$ $ds/d\eta \sim K\eta/v(\eta) \sim \eta$. Therefore, from equation (B7) it follows

$$\lim_{\eta\to 0}\frac{d\ln v}{d\eta}\frac{1}{\eta} = 0, \quad \Rightarrow \quad \lim_{\eta\to 0}\frac{d\ln v}{d\eta}\sim \eta^{1+\epsilon},\ \epsilon\geq 0. \quad \text{(B8)}$$

The behavior of the function $d\delta_b/d\xi$ is determined in a similar way, so that

$$\frac{d\delta_b}{d\xi} = \frac{d\delta_b}{ds_b}\frac{ds_b}{d\xi} = -\frac{1}{r}\frac{ds_b}{d\xi} = -\frac{K\xi}{rv_0}, \quad \Rightarrow \quad \frac{d\delta_b}{d\xi}\sim -\frac{K}{rv_0}\xi, \quad \text{(B9)}$$

where $d\delta_b/ds_b = -r = -1$ since we have chosen R as the reference length. By substituting the estimates (B8) and (B9) of the functions $d\ln v/d\eta$ and $d\delta_b/d\xi$ into the

corresponding integrals in equation (B6) and taking into account that

$$\lim_{\eta\to 0}\eta\int_0^\infty \frac{\eta'^2\,d\eta'}{(\eta'^2-\eta^2)^2}=0,\quad \text{and}\quad \lim_{\eta\to 0}\eta\int_0^\infty \frac{\xi^2\,d\xi}{(\xi^2+\eta^2)^2}=\frac{\pi}{4},$$

we obtain the result that that the curvature of the free surface at the point of flow detachment is equal to the curvature of the body, or

$$\kappa_0=\lim_{\eta\to 0}\kappa(\eta)=-1. \tag{B10}$$

References

[1] R. C. Ackerberg, The effects of capillarity on free-streamline separation. J. Fluid Mech. 70(2) (1975) 333 – 352.

[2] Ackerberg, R. C., Liu, Ta-Jo.: The effects of capillarity on the contraction coefficient of a jet emanating from a slot. Physics of Fluids 30, 289 (1987).

[3] Akselsen, A. H.: A precise conformally mapped method for water waves in complex transient environments. J. of Comput. Phys. 528, 113848 (2025).

[4] Birkhoff, G., Zarantonello, E.H.: *Jets, Wakes and Cavities*, Academic Press, New York, 1957.

[5] Brillouin, M.: Les surfaces de glissement de Helmholtz et la resistance des fluids. Ann. Chim. Phys. 23, 145 – 230 (1911).

[6] Chalikov, D., Sheinin, D.: Modeling extreme waves based on equations of potential flow with a free surface. J. of Comput. Physics 210, 247–273 (2005).

[7] Crapper, G.D.: An exact solution for progressive capillary waves of arbitrary amplitude J. Fluid Mech. 2, 532 – 540 (1957).

[8] Christodoulides, P., Dias, F.: Resonant capillary-gravity interfacial waves. J. of Fluid Mech. 265, 303 – 343 (1994).

[9] Clamond, D., Dutykh, D.: Fast accurate computation of the fully nonlinear solitary surface gravity waves, Comput. Fluids 84, 35–38 (2013).

[10] Clamond, D., Dutykh, D.: Accurate fast computation of steady two-dimensional surface gravity waves in arbitrary depth, J. Fluid Mech. 844, 491–518 (2018).

[11] Cumberbatch, E., Norbury, J.: Capillary modification of the singularity at a free-streamline separation point. Q. J. Mech. Appl. Maths. 32(3), 303 – 312 (1979).

[12] Dias, F., Iooss, G.: Capillary-gravity solitary waves with damped oscillations. Physica D: Nonlinear Phenomena 65(4), 399 – 423 (1993).

[13] Dias, F., Iooss, G.: Capillary-gravity interfacial waves in infinite depth. European J./ of Mech. B/Fluids 15(3), 367 – 393 (1996).

[14] Dias, F., Kharif, C.: Nonlinear gravity and capillary-gravity waves. Annual Review of Fluid Mechanics 31(1), 301 – 346 (1999).

[15] Duez, C., Ybert, C., Clanet, C., Bocquet, L.: Making a splash with water repellency. Nature Phys. 3, 180 – 183 (2007).

[16] Dutykh, D., Clamond, D.: Efficient computation of steady solitary gravity waves, Wave Motion. 51(1), 86–99 (2014).

[17] Dutykh, D., Clamond, D., Durán, A.: Efficient computation of capillary-gravity generalised solitary waves, Wave Motion 65, 1–16 (2016).

[18] Gurevich, M.I.: Influence of capillary forces on the jet compression coefficient. Prikl. Mat. Mekh. 25(6), 1060 – 1067 (1961). (in Russian)

[19] Gurevich, M.I.: *Theory of Jets in Ideal Fluids.* Academic. New York (1965).

[20] Helmholtz, H.: Ueber discontinuirliche Flussigkeitsbewegungen. Monasber. Berlin Akad. 215 – 228 (1868).

[21] Joukowskii, N.E.: Determination of a flow by given some conditions on a streamline. J. Russian Physical and Chemical Society. XXII (1891). (in Russian)

[22] Joukovskii, N.E.: Modification of Kirchhof's method for determination of a fluid motion in two directions at a fixed velocity given on the unknown streamline. Math. Coll. 15, 121 – 278 (1890). (in Russian)

[23] Kirchoff, G.: Zur Theorie freier Flussigkeitsstrahlen. J. reine u. angew. Math. 70. 289 – 298 (1869).

[24] Kochin, N. E., Kibel, I. A., and Roze, N. V. *Theoretical Hydromechanics* Wiley Interscience, 1964, 577pp.

[25] Lamb, H.: *Hydrodynamics*. 6th Edition, Cambridge University Press, Cambridge (1975).

[26] Michell, J.H.: On the theory of free stream lines. Phil. Trans. R. Soc. Lond. A 181, 389 – 431 (1890).

[27] Milne-Thomson, L.M.: *Theoretical hydrodynamics*. Macmillan (1962).

[28] McLeod, E.B. The Explicit Solution of a Free Boundary Problem Involving Surface Tension. Journal of Rational Mechanics and Analysis 4, 557 – 567 (1955).

[29] Murashige, S., Choi, W.: A numerical study on parasitic capillary waves using unsteady conformal mapping. J. of Comput. Physics. 328, 234–257 (2017).

[30] Semenov, Y.A., Iafrati, A.: On the nonlinear water entry problem of asymmetric wedges. J. Fluid Mech. 547, 231– 256 (2006).

[31] Semenov, Y.A., Yoon, B.-S.: Onset of flow separation at oblique water impact of a wedge. Phys. Fluids 21, 112103 – 112111 (2009).

[32] Terentiev, A.G., Kirschner, I.N., Uhlman, J.S.: *The Hydrodynamics of Cavitating Flow.* Backbone Publishing Company (2011).

[33] Vanden-Broeck, J.-M. The influence of surface tension on cavitating flow past a curved obstacle. J. Fluid Mech. 133, 255 – 264 (1983).

[34] Vanden-Broeck, J.-M. Cavitating flow of a fluid with surface tension past a circular cylinder. Phys. Fluids A 3, 263 – 266 (1991).

[35] Vanden-Broeck, J.-M. Nonlinear capillary free-surface flows. J. Eng. Math. 50, 415 - 426 (2004).

[36] Villat, H.: Sur la validite des solutions de certains problemes d'hydrodynamique. J. Math. Pure Appl. 20, 231 – 290 (1914).

[37] Yoon, B.-S., Semenov, Y.A.: Capillary cavity flow past a circular cylinder. European J. of Mech. B/Fluids 28, 670 – 676 (2009).

[38] Yoon, B.-S., Semenov, Y.A.: Cavity detachment on a hydrofoil with the inclusion of surface tension effects. European J. of Mech. B/Fluids 30, 17 –25 (2009).

[39] Zhitnikov, V.P., Terent'ev, A.G.: Non-linear problem of cavitating flow around a flat plate with capillary tension on the free boundary. Hydrodynamics of bounded streams. Chuvash State University, 51 – 58 (1988). (in Russian)